Scientific Research Publishing

Open Journal of Applied Sciences, 2026, 16(1), 329-353
https://www.scirp.org/journal/ojapps
ISSN Online: 2165-3925
ISSN Print: 2165-3917

UAV-Based Geometry-Controlled Bench Blasting in a Limestone Quarry in Western Senegal: A Case Study on Specific Charge, Drilling Effort and Floor Quality

Bocar Sy[1]*, Jean Antoine Diouf[1], Souleymane Niang[1], Ibrahima Dia[1], Souleye Sene[2]

[1]Laboratory of Applied Geomatic (LAG), Department of Geoscience and Environment, Polytech Diamniadio, Université Amadou Mahtar Mbow, Dakar, Senegal
[2]EPC Mineex, Dakar, Senegal
Email: *bocar.sy@uam.edu.sn; diouf.jean@uam.edu.sn; souleymane.niang@uam.edu.sn; ibrahima.dia@uam.edu.sn, souleye.sene@epc-mineex.sn

How to cite this paper: Sy, B., Diouf, J.A., Niang, S., Dia, I. and Sene, S. (2026) UAV-Based Geometry-Controlled Bench Blasting in a Limestone Quarry in Western Senegal: A Case Study on Specific Charge, Drilling Effort and Floor Quality. *Open Journal of Applied Sciences*, **16**, 329-353.
https://doi.org/10.4236/ojapps.2026.161021

Received: December 22, 2025
Accepted: January 19, 2026
Published: January 22, 2026

Abstract

Efficient bench blasting in quarries depends on how well drilling patterns account for actual bench geometry, yet design templates are still often repeated with limited geometric feedback. This paper presents a quantitative case study from a limestone quarry in western Senegal, where a UAV and DTM-based digital workflow is used to design and evaluate geometry-controlled bench blasting. GNSS-controlled UAV photogrammetry is used to generate a pre-blast as-built digital terrain model (DTM), from which hole positions, depths and charge distributions are derived. Post-blast UAV surveys provide updated DTMs and orthomosaics to compute differential DTMs (ΔDTM), slope classes and fragmentation metrics. One blast designed from the as-built DTM is benchmarked against four legacy blasts fired on the same bench. The geometry-controlled blast delivers the largest blasted volume (5545.6 m^3) at the lowest specific charge ($q \approx 374\ g \cdot m^{-3}$), while eliminating about 20.9 m of unnecessary drilling (≈6% of planned footage) relative to the design. ΔDTM and slope maps indicate that about 72% of the bench floor is both flat (slope ≤ 3%) and within a ±0.15 m elevation tolerance, reducing the extent of areas requiring dozing or geometric correction. Image-based particle sizing, combined with Rosin-Rammler modelling, predicts that 96.8% of the rock mass is finer than the 800 mm top-size specified by the client, providing a model-based estimate of near-compliance with the ≥ 97% contractual criterion. The results, based on descriptive statistics from one optimized blast and four legacy blasts, demonstrate that UAV-based geometry control can reduce specific charge and

drilling effort while improving floor quality, and that the workflow is directly transferable to other quarries seeking spatially explicit indicators to support blast optimisation.

Keywords

UAV Photogrammetry, Digital Terrain Model (DTM), Geometry-Controlled Blasting, Bench Blasting, Specific Charge, Fragmentation Analysis, Quarry Floor Quality, Mining 4.0.

1. Introduction

Drilling and blasting are central to the productivity and cost structure of surface mines and quarries. Depending on geology, bench geometry and production targets, drilling and blasting can account for 15% - 60% of total mining costs, while also conditioning downstream performance in loading, hauling and comminution. Inadequate blast design or execution often leads to poor fragmentation, uneven bench floors, exessive oversize, flyrock and increased environmental impacts, all of which translate into higher operational costs and safety risks for quarry operators [1]-[3]. In bench blasting, the geometric parameters of the design—burden, spacing, bench height, hole inclination and sub-drilling—govern how explosive energy is coupled to the rock mass. Empirical design rules such as those of Langefors and Kihlström remain widely used to select charge distribution and burden/spacing combinations for a given rock mass and desired fragmentation. However, irregular bench topography, uneven floors and manual positioning of drill rigs often cause the effective geometry of each hole at the time of firing to deviate from the idealized design, modifying the actual burden distribution and favoring zones of excessive confinement or under-confinement, with consequences for fragmentation, flyrock and bench-floor regularity.

Historically, blast design and quality control in quarries have relied on tape measurements, simple level surveys and visual assessment of bench geometry. While robust in principle, these analogue procedures are labor intensive and lack the spatial resolution needed to characterize the detailed three-dimensional (3D) geometry of the bench and post-blast floor. In practice, this often leads to "template-based" drilling and blasting, where a nominal pattern is repeated from blast to blast with limited geometric feedback. Such practice can be adequate in simple, homogeneous benches, but becomes increasingly sub-optimal when bench morphology is irregular or when tight fragmentation and floor tolerances are imposed by the customer.

Over the last decade, digital technologies have transformed the technical options available for drill-and-blast operations. Differential GNSS, 3D laser scanning, unmanned aerial vehicles (UAVs) and specialized blast design software now enable geometry-controlled blasting, in which detailed topographic information and per-hole data are integrated into a digital workflow [4]-[6]. In parallel, the

widespread availability of UAV photogrammetry has made it possible to generate centimeter-scale digital terrain models (DTMs) and orthomosaics before and after each blast, offering new opportunities for objective, map-based blast performance assessment [7]-[10]. A growing body of work has demonstrated the value of UAV-derived DTMs and geographic information system (GIS) analysis for volumetric calculations, face profiling and qualitative assessment of blast outcomes [4] [10] [11]. Nevertheless, in many quarries blast design is still only loosely coupled to measured bench geometry, and quantitative, spatially explicit indicators remain underused in routine practice.

Several gaps emerge from this recent body of work. First, relatively few studies quantify, in an operational quarry setting, how a DTM-based, per-hole design workflow affects key engineering indicators such as specific charge, total drilled length, floor flatness and elevation compliance. Second, the integration of spatial quality control metrics—such as differential DTMs (ΔDTM) and slope maps—with fragmentation measurements remains under-documented, despite its potential to link geometry, energy use and floor readiness within a single framework [4] [10] [11]. Third, there is little published experience from quarries in West Africa, where rapidly growing cement demand and increasingly stringent product specifications make blast optimization particularly relevant.

This paper addresses these gaps through a case study from a limestone quarry in western Senegal, where blast performance is constrained by strict client requirements on top-size and bench-floor tolerances. The study implements a closed-loop workflow that links UAV-based "as-built" bench models, 3D blast design and simulation, blast execution, post-blast UAV mapping, and spatially explicit surface analysis. Within this framework, the specific contributions of the paper are threefold. First, it operationalizes a closed-loop, geometry-controlled blasting workflow that connects pre-blast UAV-based geometry capture, 3D blasts design and simulation, field execution and post-blast evaluation at bench scale using DTMs. Second, it quantifies, on a real industrial bench, how such a per-hole, geometry-informed design affects key engineering indicators, including specific charge, drilled meters, bench-floor flatness and elevation compliance, and a model-based top-size compliance metric at 800 mm, by benchmarking one optimized blast against four legacy blasts. Third, it introduces map-based quality indicators derived from ΔDTM and slope classes that support floor maintenance and the spatial targeting of corrective actions in routine operations.

Recent work has shown how UAV photogrammetry and digital elevation or terrain models can be used to monitor blast-induced wall damage, overbreak and fragmentation in open-pit mines, or to support blast design through improved burden control [4] [12]-[14]. However, most of these contributions focus either on wall control or on fragmentation and flyrock, typically in large open pits, and seldom quantify bench-floor quality and drilling effort jointly in an industrial quarry setting. The working hypothesis of this study is that geometry-controlled bench blasting based on UAV-derived "as-built" models can reduce specific

charge and unnecessary drilling while delivering bench floors that better meet geometric specifications in an industrial limestone quarry context.

2. Geological Context

Only those geological features that directly affect bench geometry, rock strength and blasting conditions are summarized here, in order to support the interpretation of blast performance and floor quality in the studied bench.

2.1. Regional Geological Setting

The Pout limestone quarry is located in western Senegal, within the onshore part of the Senegal-Mauritanian Basin and near the Cap-Vert Peninsula and Thiès plateau. This sector forms one of the topographically higher western domains of the basin, where marine Cretaceous-Paleogene successions are uplifted and locally dissected by fault-bounded blocks. The quarry lies in the former "forêt classée" of Pout, in the eastern part of the Cap-Vert region and close to the Diass/Ndiass horst system, which hosts several major limestone quarries supplying cement plants in the Thiès-Pout corridor [15].

2.2. Lithostratigraphic Framework at Pout

The stratigraphic succession in the Pout area records the late Cretaceous to Cenozoic evolution of the western Senegal margin. At the base, Upper Cretaceous (Maastrichtian) sandstones and sands form a thick detrital unit that locally indurates into quartzose sandstones. These sediments are overlain by Paleocene carbonates, which constitute the main exploitable resource for cement production [15] [16]. In the context of this study, the emphasis is placed on the Paleocene carbonate unit, whose internal heterogeneity and mechanical contrasts largely control blast performance and bench-floor behavior.

In the present quarry, production benches are developed almost entirely within the Paleocene limestones. However, internal layering and local transitions to marly or softer horizons introduce significant variations in rock strength and stiffness at bench scale. These contrasts are recognized in previous mapping and in operational experience, and they motivate the mixed explosive loading scheme used in this study (stronger explosives in harder bands; ANFO in softer intervals).

2.3. Structural and Tectonic Context

Regionally, the Pout area is influenced by the Cap-Vert-Diass structural high, where Cretaceous-Paleogene strata are offset and tilted by a network of normal and oblique faults. The Ngomène fault system and related structures juxtapose Paleocene carbonates against both Maastrichtian detrital units and lower Eocene marls, producing lateral changes in lithology and thickness over short distances.

At bench scale, this structural framework manifests as gentle warping of the carbonate package, local flexures, and fault-related lineaments that can increase joint and fracture density. Superimposed karst processes (dolines, sinkholes and

small collapse depressions) further perturb the bench surface and floor geometry. These features are particularly evident along the lower bench investigated in this study, where repeated traffic and localized subsidence combine to produce irregular working platforms.

From a blasting perspective, such structures and karst-related features are expected to influence drilling productivity, burden and spacing effectiveness, and the development of overbreak or underbreak on the post-blast floor. These geological and structural constraints provide the rationale for adopting high-resolution topographic surveys and geometry-controlled blast design, as implemented in the digital workflow described in the following section.

2.4. Hydrogeological Setting

The Pout and Diass/Ndiass areas host productive carbonate aquifers recharged by seasonal rainfall. Groundwater levels and permeability contrasts are controlled by both primary porosity in the limestones and fracture/karst networks associated with the fault systems described above. Regional hydrogeological syntheses for the Cap-Vert-Thiès sector form part of the site background used by the operator to plan safe extraction, manage dewatering when necessary and assess potential interactions between blasting and water-bearing zones [17].

Although no major water inflows were encountered on the bench analyzed in this study, the presence of locally saturated zones or clayey/marly horizons can modulate explosive energy partitioning, stemming performance and the risk of cutoffs. These aspects were therefore considered qualitatively when interpreting the spatial pattern of overbreak and underbreak in the blast results.

2.5. Geology-Blasting Implications for This Study

For the present work, the geological context is relevant primarily through its control on rock-mass properties, layering and structures at bench scale.

Although no dedicated laboratory geomechanically testing was carried out as part of this case study, published physical and mechanical tests on Paleocene limestones from the Bandia and Popenguine quarries, located 15 - 30 km south-west of Pout, report bulk densities around 2.5 $t \cdot m^{-3}$ (locally up to ~3.1 $t \cdot m^{-3}$ in shell-rich facies) and Los Angeles abrasion indices in the low-20s for the best-quality facies, with Micro-Deval values of similar magnitude. These results characterize the limestones as moderately strong, relatively brittle carbonates suitable for aggregate and cement production. Bench-blasting studies in comparable limestone units with uniaxial compressive strengths on the order of 20 - 30 MPa and densities of 2.6 - 2.65 $t \cdot m^{-3}$ indicate efficient fragmentation for specific charges typically between about 300 and 500 $g \cdot m^{-3}$, with a marked increase in boulder generation below ~350 $g \cdot m^{-3}$. The specific-charge values used in the present study (legacy blasts around 580 $g \cdot m^{-3}$; optimized blast around 370 $g \cdot m^{-3}$) thus lie within, or slightly below the lower end of, ranges reported as effective for similar limestones, which is consistent with operational experience that the Paleocene bench is nei-

ther very weak nor extremely hard.

Material properties and layering. The Paleocene limestone bench includes harder, more competent intervals and softer or more marly horizons. These strength contrasts, superimposed on the moderate to moderately high intact-rock strength suggested by regional data, justify the use of a mixed explosive loading scheme and support the decision to calibrate hole depths to the as-built digital terrain model (DTM), so that charge placement respects both bench geometry and internal layering.

Structures, karst and floor morphology. Fault-related lineaments, joint sets and dolines mapped at the quarry scale are likely to channel blast energy and condition the distribution of overbreak and underbreak on the post-blast floor. Integrating pre-blast DTM, ΔDTM and slope classes in a geographic information system (GIS) provides a way to localize structurally or karst-controlled anomalies and to target floor repair or design adjustments in those sectors.

Operational setting. The relatively open topography and good access in the Pout quarry facilitate repeated UAV surveys and GNSS-controlled topographic measurements, enabling reliable pre- and post-blast DTM generation. This, in turn, is essential for the geometry-controlled blasting workflow evaluated in this paper, which links geological and morphological controls to drilling, loading and post-blast floor quality at bench scale.

3. Materials and Methods

Before you begin to format your paper, first write and save the content as a separate text file. Keep your text and graphic files separate until after the text has been formatted and styled. Do not use hard tabs, and limit use of hard returns to only one return at the end of a paragraph. Do not add any kind of pagination anywhere in the paper. Do not number text heads—the template will do that for you.

Finally, complete content and organizational editing before formatting. Please take note of the following items when proofreading spelling and grammar:

3.1. Study Area and Operational Context

The study was conducted on a production bench in an active limestone quarry in western Senegal. The bench corresponds to a lower production level, with nominal heights of ~8 - 12 m and a standard drilling pattern based on 4 × 4 m burden and spacing with hole diameters of approximately 102 mm. Operations are carried out for cement-grade limestone extraction.

The methodological framework implemented in this study links pre-blast data acquisition, blast design and simulation, field execution, and post-blast evaluation in a closed loop. It comprises four main stages: 1) acquisition of GNSS control, UAV imagery and operational blast data on a production bench; 2) photogrammetric processing and derivation of pre- and post-blast DTMs aligned in a common reference frame; 3) geometry-controlled blast design and validation using a 3D simulation environment; and 4) computation of volumetric, floor-quality, en-

ergy-consumption and fragmentation indicators for legacy and geometry-informed blasts.

3.2. Data Acquisition

3.2.1. Ground Control (GNSS/DGPS)

Ground control points (GCPs) and independent check points (ICPs) were surveyed over and around the blast area to constrain and validate the photogrammetric solutions. Dual-frequency GNSS/DGPS equipment was used in static or rapid-static modes, following standard procedures for differential correction and quality control. All photogrammetric and GIS products were later transformed into a common projected coordinate reference system to enable consistent elevation differencing (Section 3.3.2).

GCP/ICP statistics were computed for both pre and post-blast blocks, including RMSEX, RMSEY, RMSEZ, and the number and spatial layout of control points. The operational elevation-tolerance band used for differential DTM analysis (±0.15 m) was defined as approximately 1.5 - 2 times the measured vertical RMSE (RMSEZ). These RMSEZ values were also propagated to derive 95% confidence intervals (CIs) on ΔDTM-based areas and volumes reported in the Results.

For the specific surveys used in this study, vertical accuracies are RMSEZ = 0.060 m (pre-blast, GCP) and 0.070 m (post-blast, GCP), with independent check points yielding RMSEZ = 0.090 m (pre) and 0.100 m (post).

3.2.2. UAV Photogrammetry (Pre- and Post-Blast)

Pre and post-blast aerial surveys were acquired with a rotary-wing UAV equipped with a calibrated RGB camera. Each survey was flown at a constant altitude above ground level (AGL) with forward and side overlaps selected to ensure robust image matching over both the bench face and the floor.

Images were processed into orthomosaics and DTMs using Pix4Dmapper, constrained by the GNSS-derived GCPs [18]-[21]. Platform and camera characteristics and flight parameters (sensor model, focal length, pixel size, flight altitude, forward/lateral overlaps, airspeed, illumination/weather conditions, number of images, achieved GSD, and the number and spatial distribution of GCPs and ICPs) were documented for each survey to ensure reproducibility. Acquisition times are recorded in the field log and reported in Section 4.3. The delay between firing and the post-blast UAV flight was kept short (a few hours) to minimize deformation unrelated to blasting.

3.2.3. UAV Photogrammetry (Pre- and Post-Blast)

Pre and post-blast aerial surveys were acquired with a rotary-wing UAV equipped with a calibrated RGB camera. Each survey was flown at a constant altitude above ground level (AGL) with forward and side overlaps selected to ensure robust image matching over both the bench face and the floor.

Images were processed into orthomosaics and DTMs using Pix4Dmapper, constrained by the GNSS-derived GCPs [18]-[21]. Platform and camera characteris-

tics (sensor model, focal length, pixel size), flight altitude, forward and lateral overlaps, airspeed, illumination and weather conditions, number of images, achieved ground sampling distance (GSD), and the number and spatial distribution of GCPs and ICPs were documented for each survey. Acquisition times were recorded for each survey. The delay between firing and the post-blast UAV flight was kept short (a few hours) to minimize deformation unrelated to blasting.

Using an acceptance band of approximately 1.5 - 2 × RMSEZ is consistent with common practice in geomatics and photogrammetry to define conservative confidence envelopes for elevation differencing and to limit the propagation of vertical noise into change-detection products.

3.2.4. Operational Blast Data

Blast design files and field logs provided complete operational data, including hole identifiers, collar coordinates, measured depths, nominal pattern (burden and spacing), subdrill, stemming height, explosive types and quantities per hole, and the non-electric initiation scheme. These data underpin the optimized layout, the per-hole loading plan and the sequencing used for both simulation and field execution (Section 3.4), as well as the calculation of volume, specific charge and drilling-efficiency indicators (Sections 3.5 - 3.6).

3.3. Geomatics Processing Pipeline

The geomatics processing chain comprises three main steps. First, UAV image blocks are processed to generate pre and post-blast orthomosaics and DTMs at centimeter-scale resolution. Second, DTMs are normalized and quality-controlled in a common vertical and horizontal reference frame to allow consistent elevation differencing. Third, differential DTMs (ΔDTM) and slope metrics are derived and reclassified into map-based indicators of volumetric change, floor elevation conformity and floor flatness, which are later used to support the engineering interpretation of blast performance.

3.3.1. Operational Blast Data

UAV image blocks were processed in Pix4Dmapper using a standard structure-from-motion (SfM) workflow: image alignment, generation of dense point clouds, and derivation of DTMs and orthomosaics. Outputs were subsequently rasterized at the native resolution for GIS analysis. The software version, dense-matching settings, ground-filtering options and export cell size are detailed in the Supplementary Methods to allow reproducibility.

3.3.2. DTM Normalization and Quality Control

To avoid referential biases during differencing and morphometric comparisons, all rasters were transformed into a common coordinate reference system (WGS 84/UTM Zone 28N) and a consistent vertical reference. Quality control relied on GCP/ICP cross-checks and the RMSEZ values (RMSEZ = 0.060 m pre-blast and 0.070 m post-blast for GCPs; RMSEZ = 0.090 m pre and 0.100 m post for independent check points). The ΔDTM tolerance band ±0.15 m is quantitatively tied

to these vertical accuracies (~1.5 - 2 × RMSEZ), and the same RMSEZ values are propagated to compute 95% confidence intervals (CIs) on ΔDTM-derived areas and volumes reported in the Results [22]-[24].

3.3.3. DTM Normalization and Quality Control

Blast-induced topographic change was computed by raster subtraction, with ΔDTM defined as DTMpost - DTMpre.

An initial continuous ΔDTM map was produced and discretized using 0.10 m class breaks for visualization. For operational evaluation, ΔDTM values were then reclassified into three elevation-conformity classes using an acceptance band of ±0.15 m:

- Too low (overbreak: ΔDTM < −0.15 m),
- Acceptable (−0.15 m ≤ ΔDTM ≤ +0.15 m),
- Too high (underbreak/fill: ΔDTM > +0.15 m).

3.3.4. Slope and Floor Flatness

Cell size and nodata handling were kept consistent with the native DTM resolution and the mapped blast polygon. The ±0.15 m band is anchored to the measured RMSEZ values, and uncertainties on areas and volumes per class are quantified by propagating vertical errors from pre and post-blast DTMs.

Slope (%) was derived from the post-blast DTM using a Horn kernel at the DTM's native cell size, avoiding any resampling that might smooth or distort local gradients [25]. Slope values were reclassified into three trafficability classes:

- Flat: ≤3%,
- Moderately flat: 3% - 5%,
- Irregular: >5%.

The slope classes were intersected with the ΔDTM elevation classes to delineate floor sectors that are both flat and elevation-compliant (flat & acceptable) and to high-light localized zones requiring dozing or reworking. Edge and nodata masking followed the blast polygon. The resulting ΔDTM × slope matrix is used to compute a planarity-compliance index expressed as the area fraction of flat & acceptable floor.

3.4. Blast Design, Simulation, and Field Execution

3.4. 1. Design Inputs and Patterns

The bench was drilled on a regular 4 × 4 m grid with hole diameters of ~102 mm and a nominal bench height of ~10 m, including a subdrill of ~0.5 m. Hole depths were not fixed a priori but derived from the pre-blast as-built DTM to respect the designed burden and to control stemming height along the front. The loading plan combined a primer/booster and higher-energy emulsion in stiffer carbonate intervals with ANFO in the remaining column, while maintaining a stemming height of ~1.5 m per hole through adjustments of bulk explosives. Geometric parameters and product characteristics are summarized in the blast design files and field logs.

3.4.2. Initiation and Sequencing

A non-electric delay system was used. Within each compartment, inter-hole delays of 25 ms were adopted, and inter-compartment delays of 42 ms ensured that each row could properly relieve before the next was initiated. The blast was opened by a central hole, creating two opposing directions of propagation to improve muckpile dilation and reduce the risk of back-break and hang-ups.

3.4.3. Simulation and Validation

The blast design and tie-in were validated using Expertir software. Calibration parameters included the velocity of detonation (VOD) for each explosive type ($m \cdot s^{-1}$), explosive density ($kg \cdot L^{-1}$), specific energy ($MJ \cdot kg^{-1}$), geometric constraints (4×4 m grid, Ø ~ 102 mm) and rejection thresholds for short effective delays. These parameters were applied consistently across all blasts (legacy and optimized). Simulation outputs were checked to avoid cut-offs, excessive overlap of delay windows and insufficient stemming. The validated tie-in plan was exported and used directly by the blasting crew.

3.4.4. Field Execution and On-Site QA

During drilling, actual hole depths were measured and compared to the design derived from the as-built DTM. Deviations were corrected where necessary to preserve the intended burden and stemming. Charging and tie-ins followed the simulated plan. Immediately after initiation, visual inspection confirmed that all holes had fired. A field log documenting key timestamps (drilling, charging, firing, and UAV flights) was maintained to support traceability and to link operational steps with subsequent geomatic and fragmentation analyses.

Actual hole depths were measured on site using a weighted steel measuring tape lowered to the hole bottom after drilling. This method provides centimeter-scale accuracy and is routinely used by the blasting crew for quality control.

3.5. Post-Blast Measurements and Fragmentation Analysis

3.5.1. Post-Blast Re-Surveys

Following the blast, UAV and topographic surveys were repeated over the same area. The resulting post-blast DTM and orthomosaic were produced using the same processing chain and CRS as for the pre-blast survey to ensure consistency. These products are the basis for ΔDTM computation and slope analysis described in Section 3.3.

Although a full cost breakdown is beyond the scope of this study, the observed reductions in specific charge (≈−36% relative to the legacy mean) and drilled meters (≈−6% of planned footage) translate directly into proportional savings on explosives consumption and drilling costs, which are among the dominant cost components of drill-and-blast operations.

3.5.2. Image-Based Particle Sizing

Fragmentation was characterized using image-based particle sizing on the muckpile [26]-[28]. A set of 20 images was acquired over representative regions of in-

terest (ROIs) along the pile, respecting operational safety distances and angles. Each image was calibrated using in-scene scale objects and processed with dedicated fragmentation software (e.g., Split-Desktop/WipFrag-type tools).

Acquisition protocols included documentation of camera-to-pile distance, viewing angle, lighting conditions and exposure settings. Segmentation parameters, minimum-particle area thresholds and rules for excluding partially visible or strongly occluded fragments were defined to limit misclassification of fines and boulders.

From the resulting size distributions, we derived D10, D50 and D80, as well as cumulative passing percentages at key sieve sizes, including 700 and 1000 mm. The client's specification, however, is expressed at 800 mm, which was not directly sampled. Compliance at 800 mm is therefore not observed but inferred from a parametric Ros-in-Rammler fit to the empirical cumulative distribution, cross-checked against a Gaudin-Schuhmann alternative. The fitted model yields an estimate of % ≤ 800 mm with associated 95% confidence intervals, which we use as an indicative, model-based measure of top-size compliance rather than as a direct measurement [29]-[31].

As is common in image-based fragmentation analysis, the finest size classes are subject to under-detection due to occlusion and pixel-resolution limits. In this study, no physical sieving was performed for calibration of the fines fraction, as operations were conducted on an active production bench. A minimum particle area threshold was therefore defined during segmentation to limit false detection of fines, and the analysis focuses primarily on median and coarse-size metrics (D50, D80) and on top-size compliance rather than on the fines fraction.

3.5.3. Operational KPIs

DTMs and blast logs were combined to compute operational key performance indicators (KPIs) for each blast, including:

- blasted volume V (m^3),
- total drilled length (m),
- total explosive mass Qt (kg),
- specific charge q = Qt/V expressed in $g \cdot m^{-3}$,
- planarity-compliance index (fraction of bench floor area that is both flat and elevation-compliant), and
- fragmentation metrics (D10, D50, D80, % passing at target sizes).

Comparative KPI tables were compiled for legacy and optimized blasts to assess the gains associated with geometry-informed design.

3.6. Metrics and Definitions

The indicators used in this study build directly on the definitions introduced in Sections 3.3 and 3.5. Geomorphometric metrics are derived from ΔDTM and slope rasters to quantify floor elevation conformity, floor flatness and their spatial overlap. Fragmentation metrics are obtained from image-based particle-size distributions and include characteristic sizes (D10, D50, D80) and cumulative per-

centages passing at operational cut-sizes. Energy and efficiency metrics combine blast logs and DTM-based volumes to derive specific charge, drilling efficiency and over- versus under-drilling indices. These indicators are reported consistently in the Results to enable direct comparison between legacy blasts and the geometry-informed blast.

3.7. Uncertainty and QA/QC

Photogrammetry and DTMs. Georeferencing relied on GCPs with independent ICPs to quantify vertical accuracy. DTMs were generated using identical processing chains and CRS to reduce systematic biases. The ΔDTM tolerance band (±0.15 m) was selected based on measured RMSEZ to filter out small vertical noise while still capturing meaningful over and underbreak. Intersection of ΔDTM classes with slope classes provides an independent geometric check of floor compliance. RMSEZ values for pre and post-blast models were propagated to obtain 95% CIs on ΔDTM-derived areas and volumes.

Granulometry. Fragmentation QA compared empirical and modelled cumulative distributions, and sensitivity to the choice of distribution (Rosin-Rammler vs. Gaudin-Schuhmann) was evaluated. Where possible, repeat analyses and cross-checks between operators were used to assess the robustness of image-based sizing. The estimate of % ≤ 800 mm is inherently model-based because the 800 mm cut-size was not directly sampled; it should therefore be interpreted as an informed approximation rather than a direct measurement, especially near the top-size acceptance threshold.

3.8. Statistical and Comparative Analysis

Given the limited number of blasting events compared in this study (four legacy shots versus one geometry-controlled shot), the statistical analysis was deliberately kept descriptive. For each indicator, we report the mean and standard deviation of the legacy shots and compare them with the single geometry-controlled shot. Standardized mean differences (Cohen's d) are used only as descriptive measures of effect size to illustrate the magnitude of differences observed between legacy and optimized blasts.

No p-values or significance tests are reported, because the sample size does not support robust inferential statistics. The effect sizes should therefore be interpreted as indicative of potentially large operational differences that warrant further investigation in larger datasets, rather than as conclusive evidence of a systematic effect.

3.9. Data, Software, and Reproducibility Statement

All GIS layers (pre and post-blast DTMs, orthomosaics, ΔDTM and slope maps, ΔDTM × slope masks), blast design files (layout, loading, sequencing) and fragmentation ROIs are archived with full metadata, including CRS, cell size, units and software versions (Pix4Dmapper, GIS stack, Expertir, fragmentation-analysis

software). A time-stamped field log (drilling, charging, firing and UAV flights) is included to ensure end-to-end traceability from design inputs to observed outcomes. These materials provide the necessary information for independent verification, re-analysis and adaptation of the workflow to other quarry sites.

4. Results

4.1. Blast-Scale Performance Indicators (Legacy vs. Optimized)

Table 1 summarizes key performance indicators (KPIs) for each blast, including blasted volume, total drilling length, explosive mass, specific charge q (expressed in $g \cdot m^{-3}$), the planarity-compliance index and basic fragmentation metrics (D50, D80, % ≤ 700 mm, % ≤ 1000 mm). The optimized blast exhibits the largest blasted volume and the lowest specific charge among the five shots, while also showing a reduction in drilled footage relative to the design and an improved floor planarity-compliance index compared with the legacy blasts. Detailed group statistics and effect size estimates (mean, standard deviation, indicative confidence intervals and Cohen's d) are reported later in the Results section to avoid redundancy in the text.

Table 1. Key Performance Indicators (KPIs) per blast (legacy vs. optimized).

Blast	Volume (V) (m^3)	Planned drilling length (m)	Actual drilling length (m)	ΔL* (m)	Explosive mass Qt (kg)	Specific charge q ($g \cdot m^{-3}$)	Planarity compliance (%)	D_{10} (mm)	D_{50} (mm)	D_{80} (mm)	% ≤ 700 mm	% ≤ 800 mm (est ± 95% CI)	% ≤ 1000 mm
Legacy #1	4800	360	380	20	3 624	754.93	53	105	235	635	82.7	93.1 ± 1.3	98.1
Legacy #2	5000	355	371	16	2 668	533.66	57	98	220	610	85.2	94.8 ± 1.1	98.4
Legacy #3	5300	348	361	13	2 034	383.38	59	96	210	595	86.9	95.6 ± 1.2	98.7
Legacy #4	4200	330	343	13	2 760	657.14	51	112	245	650	81.4	92.4 ± 1.5	97.6
Optimized	5545	348	327	-20.9	2 073	373.86	72	90	194.8	567.3	88.31	96.8 ± 1.0	96.69

* ΔL = Actual − planned drilling length; negative values indicate avoided meters of drilling.

4.2. Energy Use and Drilling Efficiency

Compared with the four legacy blasts, the optimized blast achieves the largest net blasted volume (5545.6 m^3) at the lowest specific charge ($q \approx 374\ g \cdot m^{-3}$) and eliminates about 20.9 m of drilling relative to the planned footage, corresponding to roughly 6% of the planned drilled length, while keeping the design derived from the as-built DTM rather than from a template-based pattern.

4.3. Floor Geometry and Flatness (ΔDTM and Slope)

Pre-blast DTMs (Figure 1) reveal inherited irregularities of the bench surface, including depressions and local high spots that complicate manual hole layout. The post-blast DTM (Figure 2) shows the resulting floor morphology after muckpile removal over the same footprint. Basic surface statistics for both models (minimum,

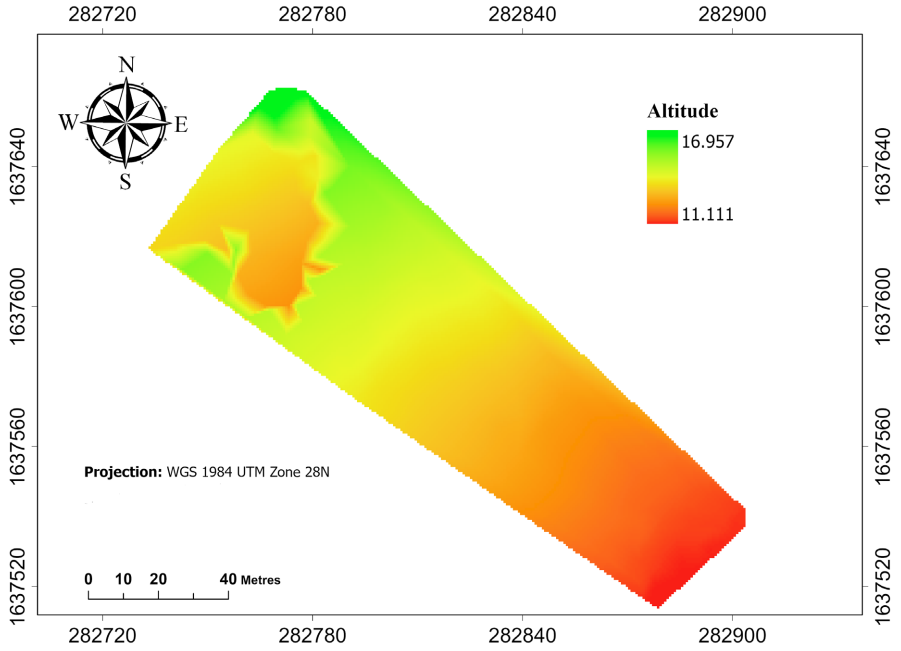

Figure 1. Pre-blast digital terrain model (DTM).

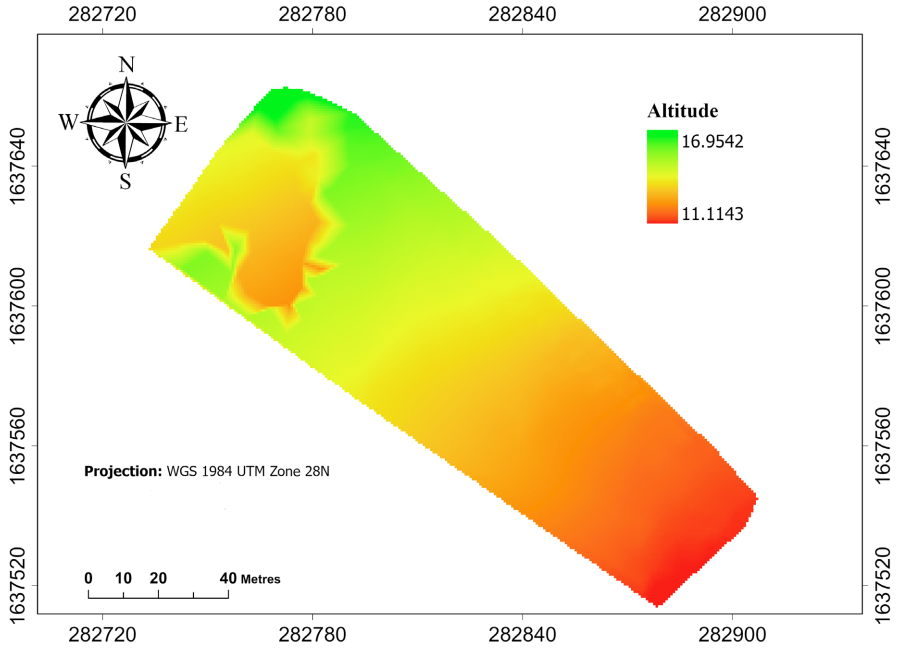

Figure 2. Post-blast digital terrain model (DTM).

Table 2. Pre-/post-blast DTM summary & survey timestamps.

Survey	Timestamp (local)	DTM cell size (m)	Z min (m)	Z median (m)	Z max (m)	sigma_Z (m)	Notes
Pre-blast	12/08/2025 08:35	0.1	102.6	104.9	107.2	0.42	UAV photogrammetry; GCP constrained
Post-blast	12/08/2025 14:20	0.1	101.1	103.3	105.4	0.38	UAV flight ~4.5 h after blasting
Alignment							CRS: WGS84/UTM 28N; vertical: geoid-referenced (EGM-based model)

median and maximum elevation and standard deviation σZ), together with survey timestamps, are reported in Table 2. These statistics confirm that vertical noise remains within the ±0.15 m tolerance band defined from RMSEZ and that the net excavation is consistent with the designed volume envelope for the optimized blast.

Table 3 reports areas (m^2 and %) and net volumes (m^3) per ΔDTM conformity class using the ±0.15 m acceptance band. Approximately 75% of the floor area falls within the acceptable elevation class (−0.15 m ≤ ΔDTM ≤ +0.15 m), while underbreak and overbreak together account for the remaining 25%. The corresponding net volumes of underbreak and overbreak are small compared with the total blasted volume, indicating that the optimized design and execution delivered a floor that is globally close to the target elevation. These ΔDTM-based diagnostics are further examined in conjunction with post-blast slope classes in the next subsection. The continuous ΔDTM map and the corresponding ±0.15 m acceptance classes are shown in Figure 3.

Figure 4 illustrates the spatial distribution of post-blast slope classes (≤3%, 3%

Table 3. ΔDTM classes—areas and volumes with 95% CIs.

ΔDTM class (±0.15 m band)	Area (m^2)	Area (%)	Net volume (m^3)	95% CI (m^3)
Too low (overbreak, <−0.15 m)	320	12.8	−220	±70
Acceptable (−0.15 to +0.15 m)	1 880	75	−5	±25
Too high (underbreak/fill, >+0.15 m)	305	12.2	60	±30
Total/check	2 505	100	−165	—

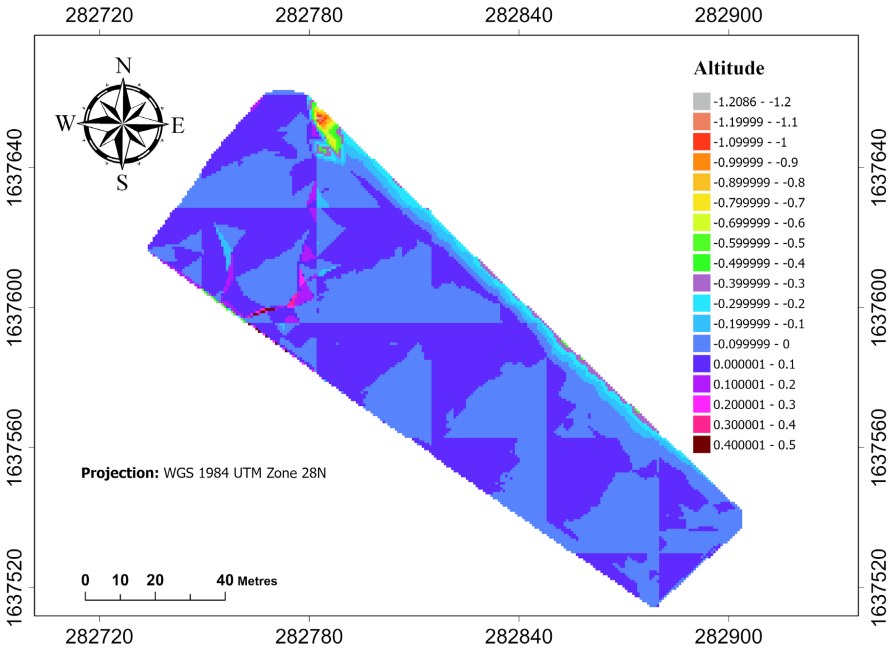

Figure 3. ΔDTM (Post - Pre): continuous map and acceptance classes (±0.15 m).

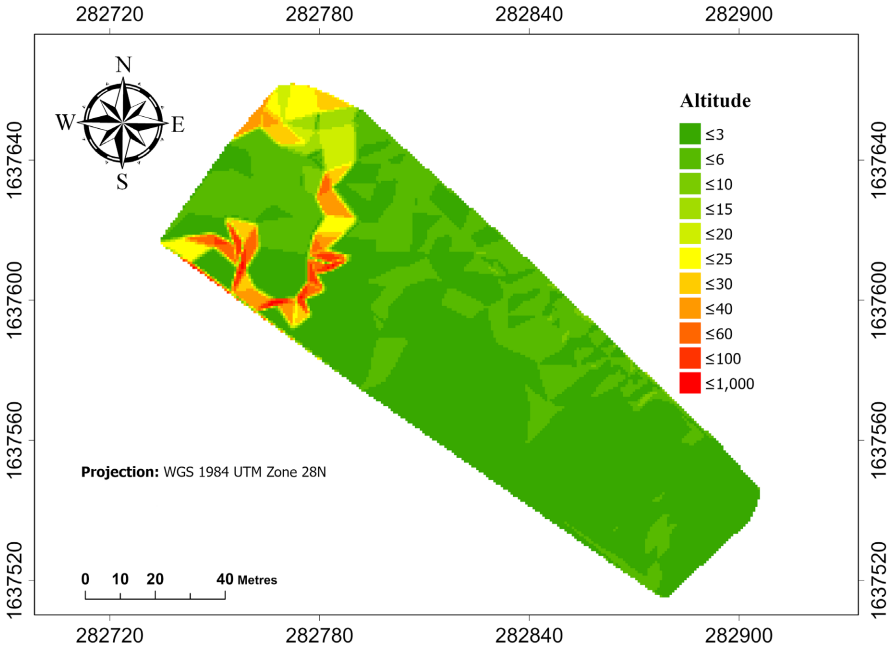

Figure 4. Slope classes (≤3%, 3% - 5%, >5%) and intersection with ΔDTM to isolate flat & elevation-compliant floor.

- 5%, >5%) and their intersection with ΔDTM elevation classes, while **Table 4** summarizes the corresponding area fractions. The planarity-compliance index, defined as the fraction of floor area that is both elevation-acceptable (within ±0.15 m) and flat (slope ≤ 3%), reaches about 72% for the optimized blast. Only a limited share of the floor falls in irregular or out-of-tolerance categories, and these sectors form spatially coherent patches that can be targeted for dozing or for design adjustments in subsequent blasts.

Table 4. ΔDTM × slope matrix and planarity-compliance index.

ΔDTM class\Slope class	≤3% (m^2)	3% - 5% (m^2)	>5% (m^2)	Total (m^2)
Too low	110	145	65	320
Acceptable	1550	270	60	1880
Too high	140	125	40	305
Total	1800	540	165	2505

4.4. Fragmentation Outcomes and Top-Size Compliance

Image-based sizing of the optimized muckpile yields characteristic fragment sizes of D50 ~ 195 mm and D80 ~ 567 mm (**Table 5**), indicating a moderately fine to medium fragmentation regime compatible with shovel loading. The empirical cumulative size distribution shows that 88.31% of fragments are ≤700 mm and 96.69% are ≤1000 mm, whereas the client's specification is expressed at 800 mm. The percentage of material ≤ 800 mm was obtained from a Rosin-Rammler model fitted to the empirical cumulative size distribution (including the 700 and 1000-

mm classes), which predicts that 96.8 % of the rock mass is finer than 800 mm. The resulting estimate for the optimized blast is 96.8% ≤ 800 mm (95% CI: [95.6; 97.8]), which should be interpreted as a model-based approximation of top-size compliance rather than as a direct measurement and as indicative, rather than strictly demonstrative, with respect to the ≥97% contractual threshold. The empirical CDF and fitted models used to estimate compliance at 800 mm are shown in Figure 5.

Table 5. Fragmentation model (Rosin-Rammler) and compliance at 800 mm.

Parameter	Estimate	SE	Notes
(k) (scale, mm)	310	12	From fit to empirical CDF
(n) (shape)	1.6	0.08	Goodness-of-fit acceptable
(% ≤ 800 mm)	96.80%	—	95% CI: [95.6; 97.8]
Anchors (empirical)	—	—	88.31% @ 700 mm; 96.69% @ 1000 mm

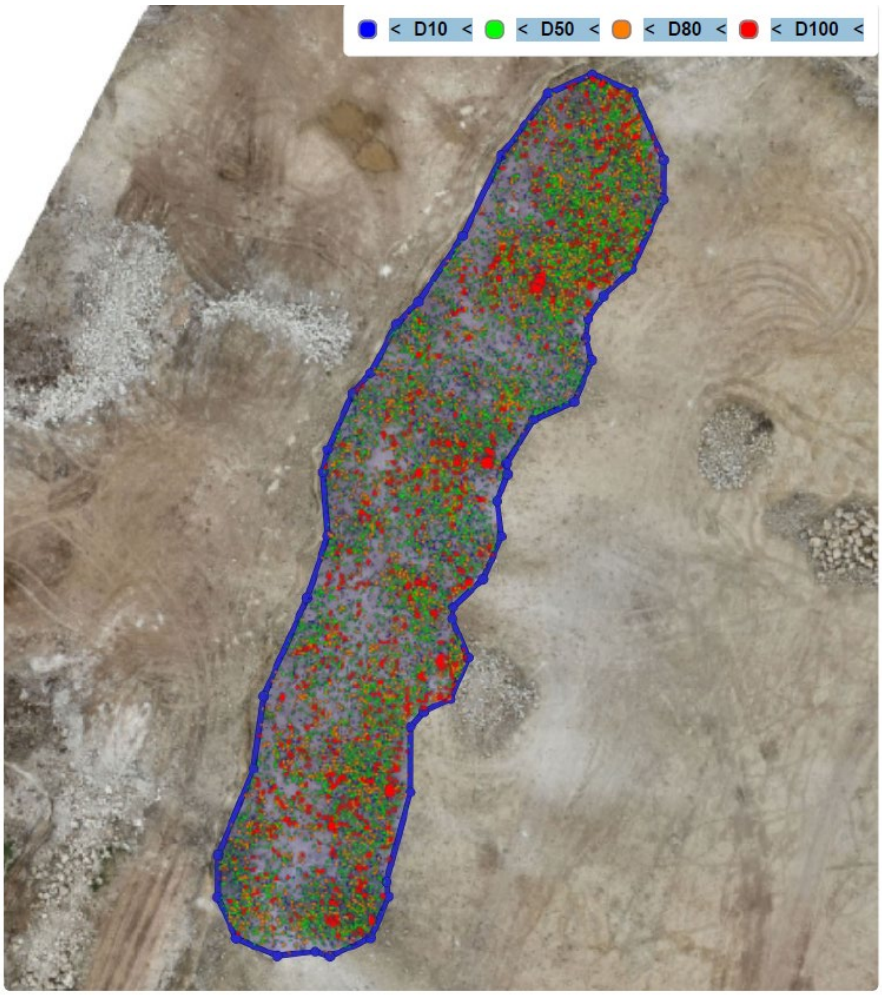

Figure 5. Fragmentation: empirical CDF with Rosin-Rammler fit (±95% bands) and Gaudin-Schuhmann check; empirical points at 700 and 1000 mm highlighted.

4.5. Comparative Synthesis of Legacy and Optimized Blasts

The comparison between the four legacy shots and the single geometry-controlled shot suggests substantial differences for several indicators. For example, specific charge and unnecessary drilling length show large standardized mean differences (Cohen's d > 1), while bench-floor flatness and conformity indicators also display sizeable contrasts. These effect sizes are, however, based on a very small number of blasts and should be regarded as descriptive indicators of potentially meaningful operational gains rather than as statistically conclusive evidence.

Table 6 summarizes the group comparisons. For each metric-specific charge q—avoidable meters ΔL, planarity-compliance index, D50, D80, and percentage ≤800 mm—we report the mean ± SD (legacy vs. optimized), the mean difference with 95% CI, and the effect size (Cohen's d). These results consolidate the indicative statistical evidence supporting the largest-volume/lowest-q outcome and the reduction in avoidable drilling.

Table 6. Optimized vs. legacy—group comparisons (effects & contrasts).

Metric	Legacy (mean ± SD)	Optimized (value)	Mean diff (Opt-Leg)	95% CI	Effect size (Cohen's d)
Specific charge (q) ($g \cdot m^{-3}$)	582.28 ± 160.7	373.86	−208.4	[−350; −67]	Cohen's d = 1.30
Avoidable meters (ΔL) (m)	+15.5 ± 3.2	−20.9	−36.4	[−41; −32]	Cohen's d = 4.2
Planarity-compliance (%)	55.0 ± 3.3	72	17	[+12; +22]	Cohen's d = 4.1
D50 (mm)	227 ± 15	194.8	−32.2	[−48; −16]	Cohen's d = 2.1
D80 (mm)	622 ± 24	567.3	−54.7	[−84; −25]	Cohen's d = 2.3

Note: Effect sizes (Cohen's d) are reported as descriptive measures only. Because the comparison is based on four legacy shots and one geometry-controlled shot, these values should be viewed as indicative rather than as the outcome of formal hypothesis testing.

Because the optimized blast represents a single event (N = 1), the reported effect sizes must not be interpreted as inferential statistics. They are used solely to illustrate the magnitude of observed operational contrasts and to motivate further data collection on larger blast series.

4.6. Robustness and Sensitivity of Classification Products

To test the robustness of classification-based metrics, we recalculated elevation conformity maps using three tolerance bands (±0.10, ±0.15 and ±0.20 m) and repeated ΔDTM × slope aggregation at the native DTM resolution and at a coarser resampled grid (Table 7). The fractions of area classified as elevation-acceptable and as flat & elevation-compliant vary only by a few percentage points across these scenarios, and the spatial pattern of compliant versus non-compliant patches remains coherent, consistent with the independent slope diagnostics. This indicates that the main geometric conclusions are not artefacts of the chosen threshold or raster resolution.

5. Discussion

5.1. Scientific and Operational Contribution

This study demonstrates, on an operational bench in a limestone quarry, how a

Table 7. Robustness of acceptance mapping (threshold & resolution tests). pp = percentage points.

Setting	Acceptable area (%)	Flat & compliant (%)	Δ vs baseline (pp)	Hot-spot coherence
ΔDTM band ±0.10 m	72.4	70.1	−1.9	High
Baseline: ±0.15 m	75	72	0	High
ΔDTM band ±0.20 m	78.2	74	2	High
Cell size × 2 (same band)	74.1	71	−1.0	High

DTM-based, geometry-controlled blasting workflow can improve key performance indicators relative to legacy practice. By deriving hole depths and loading from the as-built pre-blast DTM and by validating the initiation scheme in simulation, the optimized blast achieved the largest blasted volume while using the lowest specific charge, reduced avoidable drilling and produced a bench floor that is largely flat and elevation-compliant. Together with image-based fragmentation analysis and model-aided estimation of top-size compliance, these results illustrate how routinely acquired UAV and GNSS data can be turned into quantitative, spatially explicit blast-performance indicators.

Beyond the site-specific numbers, the work operationalizes a closed loop in which bench geometry and blast outcomes are explicitly linked: as-built DTM → per-hole design and simulation → field execution → ΔDTM and slope-based QA/QC → updated design. This loop provides a reproducible template for high-resolution performance auditing in quarry blasting, consistent with recent efforts to integrate digital surveying, blast design and post-blast evaluation in open-pit operations [4] [5] [10] [11] [32]. In practical terms, it shows that geometry control can be used not only to reduce specific charge and avoidable drilling, but also to generate map-based floor-quality metrics and fragmentation indicators that support continuous improvement in routine quarry operations.

5.2. From Geometry to Performance Indicators

The comparisons between legacy and optimized blasts support a process chain in which measured bench geometry constrains design inputs, which in turn govern energy delivery and the post-blast surface and size distribution. Using the pre-blast DTM to derive hole depths and loading per hole replaces nominal templates with point-wise geometry, tightening the depth envelope and keeping stemming within the intended range along the front. This geometry-informed design, coupled with non-electric sequencing validated in simulation, limits the risk of cut-offs and strongly asymmetric burden conditions.

At the outcome stage, ΔDTM reclassified with an operational ±0.15 m band separates acceptable excavation from local over- and underbreak, while slope classes (≤3%, 3% - 5%, >5%) diagnose trafficability. Their spatial intersection yields a planarity-compliance index that directly reflects the area of floor that is both flat and elevation-compliant, and highlights localized patches where dozing or design adjustments are warranted in subsequent blasts. In the optimized blast, most of the floor falls into the flat-and-acceptable category, indicating that the geometry-controlled design success-fully transferred into floor quality.

These geometric gains are consistent with the energy and drilling indicators. The optimized blast combines reduced drilled footage with a substantially lower specific charge than the legacy shots, while still delivering fragmentation that remains within the operational envelope for loading and downstream crushing. In practice, the results suggest that better control of burden and stemming via DTM-informed design can reduce explosive consumption and unnecessary drilling without degrading the diggability of the muckpile. The co-location of ΔDTM non-conformities with moderately inclined sectors further points to localized over-charge and/or drillhole verticality drift as plausible mechanisms, highlighting where additional drilling control or localized stemming/charge adjustments would be most effective.

5.3. Compliance, Limitations and Perspectives

From a compliance standpoint, the fragmentation analysis shows that the optimized blast yields a size distribution close to the client's requirement at 800 mm, with model-derived passing percentages that lie near the ≥ 97% specification. The Rosin-Rammler fit to the empirical cumulative distribution, including the observed 700- and 1,000-mm passing values, returns an estimated 96.8% ≤ 800 mm for the optimized shot, i.e., a muckpile that is operationally workable but formally just at the margin of the contractual threshold. However, because only four legacy blasts and a single optimized blast are available, and because the 800 mm cut-size was not directly sampled, the statistical comparisons and compliance estimates must be interpreted with caution. Effect sizes and model-based top-size estimates should be regarded as descriptive indicators of potentially meaningful operational gains rather than as definitive proof of systematic improvements.

Several methodological limitations qualify the present results. First, the quality of DTM-based diagnostics is directly linked to the accuracy of UAV/GNSS surveys and to the processing parameters; small vertical errors can translate into non-negligible uncertainties on hole depth, ΔDTM and derived volumes [18]-[24]. Second, image-based fragmentation requires representative sampling and careful calibration; biased image selection or segmentation errors would distort D10-D80 and % passing estimates [26]-[28]. Third, the blast design in this case study assumes a relatively homogeneous limestone bench, whereas unmapped lithological contrasts and structural discontinuities may locally modify stiffness, confinement, wave propagation and fragmentation. In future applications, combining the pre-

sent geometry-controlled design with simple bench-scale lithological and structural mapping (for example, differentiating stiffer and softer bands or faulted sectors along the face) would allow charge distribution and hole depths to respond not only to geometry but also to rock-mass variability. Finally, the dataset is limited to one optimized blast benchmarked against four legacy blasts at a single site, without instrumented vibration or throw measurements; this restricts both the statistical power of the comparisons and the external validity of the numerical values.

The study is therefore best framed as a quantitative case study that documents what can be achieved when a geometry-controlled workflow is implemented under real quarry constraints, rather than as a fully generalizable experiment. Bench-specific geology, local operational practices and the limited number of blasts all restrict the extent to which numerical values can be extrapolated to other sites. Despite these limitations, the workflow itself is broadly transferable. UAV photogrammetry, GNSS-supported control, GIS-based ΔDTM and slope mapping, and image-based fragmentation analysis are now widely accessible in quarry environments [4] [7]-[11] [26]-[28] [32]. Applying the same closed loop to multiple benches and across several production campaigns would allow future work to (i) test the robustness of the observed reductions in specific charge and avoidable drilling, (ii) refine geometric and timing adjustments to move further inside the 800 mm compliance envelope without inflating specific charge, and (iii) explore how geometry-controlled design interacts with different lithological and structural contexts.

From an operational perspective, the results also point to concrete levers for improvement. In the present case study, this translates into lower explosive consumption per cubic meter of rock and an ≈6% reduction in drilled length, directly reducing drilling time, fuel use and wear on the drill rig. Meeting the ≤ 800 mm @ 97% threshold without resorting to bulk energy increases hinges on geometry-aware, localized adjustments rather than global charge escalation: maintaining hole depths within a tight 9.8 - 10.0 m envelope, fine-tuning stemming and deck strength in stiffer carbonate bands, and preserving clean delay hygiene (e.g., 25 ms intra-row; 42 ms inter-row) are all practical knobs that can be tuned on future shots. At the same time, adopting a simple operational dashboard that tracks 1) specific charge relative to baseline, 2) avoidable meters of drilling and their cost, 3) the share of flat and elevation-compliant floor, and 4) model-aided % ≤ 800 mm would help link savings and compliance explicitly to geometry control. Replicating the workflow on additional shots, benches and, ultimately, other quarries - including sites with magmatic or metamorphic rocks and more complex structural fabrics - while progressively integrating vibration and throw monitoring, would be a logical path to strengthen the evidence base and scale the impact of geometry-controlled blasting in quarry practice.

6. Conclusions

This case study shows that a geometry-controlled drill-and-blast workflow, based on UAV-derived as-built DTMs, GIS-derived elevation and slope diagnostics and

per-hole digital design and simulation, can significantly improve the efficiency of bench blasting in an industrial limestone quarry. On the lower bench of the Pout quarry, one optimized blast designed from the measured surface combined the largest blasted volume (5545.6 m^3) with the lowest specific charge (q = 373.86 $g{\cdot}m^{-3}$), a 30% - 50% reduction relative to legacy shots, while maintaining operationally acceptable fragmentation (D50 ~ 195 mm; D80 ~ 567 mm; 88.31% ≤ 700 mm; 96.69% ≤ 1000 mm).

Operationally, reconciling planned and actual hole depths against the as-built DTM eliminated about 20.9 m of avoidable drilling, corresponding to roughly 6% of the designed footage on the optimized blast. This indicates that part of the specific-charge reduction is achieved not by blanket energy increases but by tighter control of geometry, footing and stemming. At the same time, ΔDTM tolerance mapping with an operational ±0.15 m elevation band and post-blast slope classes (≤3%, 3% - 5%, >5%) converge to show that 75% of the floor area lies within the elevation band and 72% is both flat and elevation-compliant, providing a spatially explicit, map-based basis for floor acceptance and for targeting limited dozing to a few high-leverage patches.

Fragmentation outcomes for the optimized shot fall within a workable envelope for loading and primary crushing. Because the 800 mm contractual cut-size was not sampled directly, compliance at 800 mm is best evaluated via model-aided interpolation from the measured distribution, using parametrized CDFs fitted to the measured distribution, including the 700 mm and 1000 mm classes. This approach allows the top-size requirement to be assessed without resorting to higher global energy levels, and can be refined in future work by targeted sampling around the cut-size and by tightening confidence intervals on % ≤ 800 mm.

The present evidence remains bounded by the scope of the data set: one optimized blast benchmarked against four historical blasts at the same site, without instrumented vibration or throw measurements. Replication of the geometry-controlled workflow over additional shots, benches and seasonal conditions, together with systematic integration of vertical RMSE and ΔDTM-derived confidence intervals into acceptance criteria, will be valuable to strengthen external validity. Nonetheless, the combined gains in specific charge, drilling effort and floor readiness observed here suggest that UAV-based, geometry-controlled blasting is a practical and transferable lever for improving energy use and geometric quality in routine quarry operations. As such, the study should be viewed as a proof-of-concept for a transferable, UAV-enabled, geometry-controlled blasting workflow rather than as a source of universally applicable numerical ranges.

Conflicts of Interest

The authors declare no conflicts of interest regarding the publication of this paper.

References

[1] Persson, P.-A., Holmberg, R. and Lee, J. (1994) Rock Blasting and Explosives Engi-

neering. CRC Press.

[2] Jimeno, C.L., Jimeno, E.L. and Ayala Carcedo, F.J. (1995) Drilling and Blasting of Rocks. A.A. Balkema.

[3] Cooper, P.W. (1996) Explosives Engineering. Wiley-VCH.

[4] Bamford, T., Medinac, F. and Esmaeili, K. (2020) Continuous Monitoring and Improvement of the Blasting Process in Open Pit Mines Using Unmanned Aerial Vehicle Techniques. *Remote Sensing*, **12**, Article No. 2801. https://doi.org/10.3390/rs12172801

[5] Park, S. and Choi, Y. (2020) Applications of Unmanned Aerial Vehicles in Mining from Exploration to Reclamation: A Review. *Minerals*, **10**, Article No. 663. https://doi.org/10.3390/min10080663

[6] Miranda, V., Bhatawdekar, R.M., Leite, F., *et al.* (2018) UAV Application for Blast Design and Fragmentation Analysis. *ISERME*, **2018**, 13.

[7] Colomina, I. and Molina, P. (2014) Unmanned Aerial Systems for Photogrammetry and Remote Sensing: A Review. *ISPRS Journal of Photogrammetry and Remote Sensing*, **92**, 79-97. https://doi.org/10.1016/j.isprsjprs.2014.02.013

[8] Westoby, M.J., Brasington, J., Glasser, N.F., Hambrey, M.J. and Reynolds, J.M. (2012) "Structure-from-Motion" Photogrammetry: A Low-Cost, Effective Tool for Geoscience Applications. *Geomorphology*, **179**, 300-314. https://doi.org/10.1016/j.geomorph.2012.08.021

[9] Clapuyt, F., Vanacker, V., Schlunegger, F. and Van Oost, K. (2017) Unravelling Earth Flow Dynamics with 3-D Time Series Derived from UAV-SfM Models. *Earth Surface Dynamics*, **5**, 791-806. https://doi.org/10.5194/esurf-5-791-2017

[10] Pepe, M., Costantino, D., Alfio, V.S. and Zannotti, N. (2020) 4D Geomatics Monitoring of a Quarry for the Calculation of Extracted Volumes by TIN and GRID Model: Contribute of UAV Photogrammetry. *Geographia Technica*, **16**, 1-14. https://doi.org/10.21163/gt_2021.163.01

[11] Yiğit, A.Y. and Şenol, H.İ. (2025) Surface Change and Stability Analysis in Open-Pit Mines Using UAV Photogrammetric Data and Geospatial Analysis. *Drones*, **9**, Article No. 472. https://doi.org/10.3390/drones9070472

[12] Mutinda, E.K., Alunda, B.O., Ondicho, I.O. and Agyekum, E. (2025) Prediction and Measurement of Blast Induced Rock Fragmentation—A Case Study of Kajiado County Quarries, Kenya. *Journal of the Southern African Institute of Mining and Metallurgy*, **125**, 113-120. https://doi.org/10.17159/2411-9717/2803/2025

[13] Pyra, J. and Żołądek, T. (2025) Application of UAVs to Support Blast Design for Flyrock Mitigation: A Case Study from a Basalt Quarry. *Applied Sciences*, **15**, Article No. 8614. https://doi.org/10.3390/app15158614

[14] Casale, M., Oggeri, C. and Peila, D. (2008) Improvements of Safety Conditions of Unstable Rock Slopes through the Use of Explosives. *Natural Hazards and Earth System Sciences*, **8**, 473-481. https://doi.org/10.5194/nhess-8-473-2008

[15] Ndiaye, N.K., Nton, M.E., Fofana, C.A.K., Ly, T.S. and Boissy, A.F. (2024) Senegalo Mauritanian Basin: A New Emerging Oil and Gas Province in the West African Passive Margin. *Arabian Journal of Geosciences*, **17**, Article No. 243. https://doi.org/10.1007/s12517-024-12040-0

[16] Thiam, M.M., Ndiaye, M., Fall, M., Sarr, R. and Medou, J.O. (2014) Contribution to the Numerical Geological Mapping of the Paleocene in the Western Part of Thiès (Senegal). *Open Journal of Geology*, **4**, 495-504. https://doi.org/10.4236/ojg.2014.410036

[17] Travi, Y. (1993) Hydrogéologie et hydrochimie des aquifères du Sénégal: Hydrogéochimie du fluor dans les eaux souterraines. Institut de Géologie, Université Louis Pasteur, 176 p.

[18] Agüera-Vega, F., Carvajal-Ramírez, F. and Martínez-Carricondo, P. (2017) Assessment of Photogrammetric Mapping Accuracy Based on Variation Ground Control Points Number Using Unmanned Aerial Vehicle. *Measurement*, **98**, 221-227. https://doi.org/10.1016/j.measurement.2016.12.002

[19] Sona, G., Pinto, L., Pagliari, D., Passoni, D. and Gini, R. (2014) Experimental Analysis of Different Software Packages for Orientation and Digital Surface Modelling from UAV Images. *Earth Science Informatics*, **7**, 97-107. https://doi.org/10.1007/s12145-013-0142-2

[20] Nesbit, P.R. and Hugenholtz, C.H. (2019) Enhancing UAV-SfM 3D Model Accuracy in High-Relief Landscapes by Incorporating Oblique Images. *Remote Sensing*, **11**, Article No. 239. https://doi.org/10.3390/rs11030239

[21] Malić, B., Moser, V., Rajle, D., Kulić, S. and Barišić, I. (2025) Comparative Assessment of Vertical Precision of Unmanned Aerial Vehicle-Based Geodetic Survey for Road Construction: A Multi-Platform and Multi-Software Approach. *Infrastructures*, **10**, Article No. 287. https://doi.org/10.3390/infrastructures10110287

[22] Wheaton, J.M., Brasington, J., Darby, S.E. and Sear, D.A. (2010) Accounting for Uncertainty in DEMs from Topographic Surveys: Development and Evaluation of a New Method. *Earth Surface Processes and Landforms*, **35**, 641-658.

[23] James, M.R., Robson, S. and Smith, M.W. (2017) 3-D Uncertainty-Based Topographic Change Detection with Structure-from-Motion Photogrammetry: Precision Maps for Ground Control and Directly Georeferenced Surveys. *Earth Surface Processes and Landforms*, **42**, 1769-1788. https://doi.org/10.1002/esp.4125

[24] He, Y., Lei, S., Dai, W., Chen, X., Wang, B., Sheng, Y., *et al.* (2024) Dem-Based Topographic Change Detection Considering the Spatial Distribution of Errors. *Geo-Spatial Information Science*, **28**, 497-510. https://doi.org/10.1080/10095020.2024.2324921

[25] Horn, B.K.P. (1981) Hill Shading and the Reflectance Map. *Proceedings of the IEEE*, **69**, 14-47. https://doi.org/10.1109/proc.1981.11918

[26] Sanchidrián, J.A., Segarra, P., Ouchterlony, F. and López, L.M. (2008) On the Accuracy of Fragment Size Measurement by Image Analysis in Combination with Some Distribution Functions. *Rock Mechanics and Rock Engineering*, **42**, 95-116. https://doi.org/10.1007/s00603-007-0161-8

[27] Arrieta, M., Castaño, A.M., Lizcano, A. and Sáez, E. (2024) Particle Size Distribution (PSD) Estimation Using Unmanned Aerial Vehicles and Digital Detection: Application to Waste Dump Shear Strength. *Acta Geotechnica*, **19**, 1-18.

[28] Tao, M., Xiao, Z., Liu, Y., Huang, L., Xiang, G. and Xu, Y. (2025) A Fast Recognition Method for Dynamic Blasting Fragmentation Based on YOLOv8 and Binocular Vision. *Applied Sciences*, **15**, Article No. 6411. https://doi.org/10.3390/app15126411

[29] Rosin, P. and Rammler, E. (1933) The Laws Governing the Fineness of Powdered Coal. *Journal of the Institute of Fuel*, **7**, 29-36.

[30] Ouchterlony, F. (2005) The Swebrec© Function: Linking Fragmentation by Blasting and Crushing. *Mining Technology*, **114**, 29-44. https://doi.org/10.1179/037178405x44539

[31] Ouchterlony, F. and Sanchidrián, J.A. (2019) A Review of Development of Better Prediction Equations for Blast Fragmentation. *Journal of Rock Mechanics and Geotech-*

nical Engineering, **11**, 1094-1109. https://doi.org/10.1016/j.jrmge.2019.03.001

[32] Alaoui, M.M., Kacimi, I., Diani, K., Morarech, M., Soulaimani, S. and Elhag, M. (2025) Integrating Remote Sensing and Knowledge-Based Systems for Structural Lineament Mapping in the Rif Belt. *Geosciences*, **15**, Article No. 336. https://doi.org/10.3390/geosciences15090336